

Cooperative Multi-Static Target Localization for ISAC in Cluttered Industrial IoT Networks

Mostafa Nozari, Israel Leyva-Mayorga, and Gilberto Berardinelli

Department of Electronic Systems, Aalborg University, Denmark ({mnozari, ilm, gb}@es.aau.dk)

Abstract—In this paper, we propose a novel integrated sensing and communications (ISAC) framework for collaborative multi-static target localization in dense Industrial Internet-of-Things (IIoT) environments in the presence of environmental clutter. We first develop a lightweight temporal clutter-suppression learning method to mitigate persistent reflections. Building on this, we propose an iterative localization algorithm that integrates two key components introduced in this work: a sampling-based field-of-view-aware initialization (SFI) scheme and an empirical position error bound (PEB) scheme, which together adaptively identify the most informative subset of sensing nodes. A reliability-aware weighted least-squares estimator is then employed to fuse range and angle-of-arrival measurements from the selected sensing receivers for target localization. Numerical results demonstrate rapid convergence of the proposed method, reducing the localization RMSE by nearly two orders of magnitude within six sensing iterations to about 45 cm, while significantly outperforming all considered benchmarks under the same sensing-resource budget.

Index Terms—Integrated sensing and communication (ISAC), Cooperative localization, Clutter suppression, Node selection.

I. INTRODUCTION

In the 6G era, in-X subnetworks (SNs) are autonomous wireless networks embedded within physical entities, such as vehicles, robots, and production modules, where they support communication among internal components. In mission-critical industrial environments, their dense deployment makes it challenging to satisfy stringent latency and reliability requirements under a high degree of autonomy. Therefore, they must combine robust standalone operation with seamless integration into the 6G infrastructure for coordination, computation offloading, and resource management [1].

Integrated sensing and communication (ISAC) has emerged as a promising technology for next-generation wireless networks by enabling dual use of spectrum, hardware, and signaling for both data transmission and environmental sensing. In dense 5G/6G deployments, such a unified infrastructure can evolve into a perceptive network, where spatially distributed nodes, such as industrial internet of things (IIoT) SNs, collaboratively provide diverse observation perspectives for tasks, including detection, localization, tracking, and mapping.

Cooperative sensing, especially in scenarios with spatially distributed nodes, has recently emerged as a promising research direction in ISAC, where measurements from multiple nodes are utilized to improve sensing accuracy [2], [3]. However, adaptively selecting a limited subset of nodes that provides rich geometric diversity from a large pool of candidates, remains an open challenge.

Recent SN studies have mainly focused on communication aspects such as resource management and interference coordination [4], [5]. In our previous work [2], SNs were considered for radio sensing, where informative SNs were selected to cooperatively sense the environment and share range measurements at the edge server (ES) for target localization under Gaussian and fading channels. However, this framework did not incorporate angle of arrival (AoA) measurements and was not designed for radar cross section (RCS)-agnostic localization. Moreover, the monostatic transmitter (Tx)–receiver (Rx) co-location constraint limits geometric diversity and typically requires sophisticated self-interference cancellation.

Sensing in cluttered environments, with potentially strong interference scattered from surrounding objects, is challenging. While some of ISAC studies assumes idealized clutter-free sensing [6], other rely on clutter mitigation through separability assumptions and statistical signatures. A practical alternative is Doppler-domain moving target indication (MTI)/high-pass filtering [7]. However, it can create blind Doppler regions.

This paper proposes a novel multi-static sensing framework for target localization in a dense cluttered IIoT scenario under imperfect channel state information (CSI), where the most informative subset of collaborative SNs is dynamically selected to improve localization accuracy with limited latency. The main contributions are as follows:

- We propose a novel cooperative sensing framework for ISAC operating in a bi-/multi-static sensing configuration that is applicable to practical scenarios with environmental clutter and imperfect CSI.
- We develop a lightweight and model-agnostic clutter-suppression learning method based on temporal background estimation, which does not rely on explicit clutter-power modeling or motion-based filtering assumptions.
- We propose a node-selection and reliability-aware fusion scheme that combines a sampling-based field of view (FoV)-aware initialization with empirical Position error bound (PEB)-based node selection. This approach maximizes geometric visibility and identifies the most informative sensing links. The selected links provide time of arrival (ToA) and AoA measurements, which are jointly fused via a weighted least square (WLS) estimator. The empirical Cramér–Rao lower bound (eCRLB) models are used to weight the reliability of each measurement.
- We evaluate the proposed method under clutter-free, clutter-suppressed, and cluttered conditions against theoretical and empirical benchmarks, and analyze localiza-

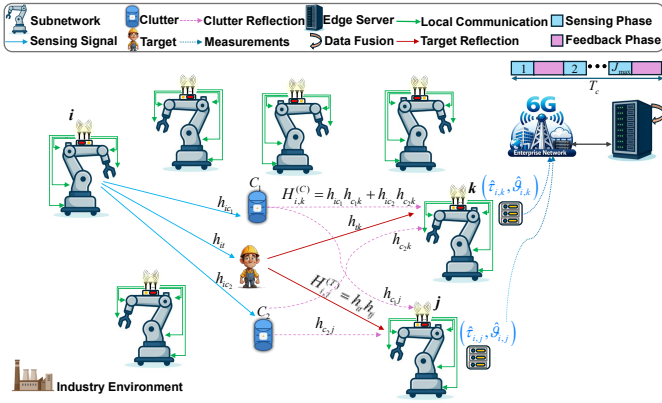


Fig. 1: Dense IIoT factory with N SNs supporting local downlink communication while collaboratively localizing a target via multi-static OFDM sensing.

tion accuracy and latency–communication trade-offs for varying antenna and multi-static receiver counts.

II. SYSTEM MODEL

We consider an IIoT network consisting of an ES and N spatially distributed SNs with communication and sensing capabilities, which cooperate to enable on-demand target localization for monitoring and safety purposes, as illustrated in Fig. 1. The ES orchestrates sensing-communication operations, manages resource allocation across SNs, and performs centralized data fusion. Each SN $n \in \mathcal{N} \triangleq \{1, \dots, N\}$ contains a single access point (AP) that primarily serves a set of single-antenna users, while also supporting radar sensing and cooperating in a bi-/multi-static manner. Each AP is equipped with a uniform-linear array (ULA) with M_a antenna elements with inter-element spacing $d \leq \lambda/2$, where λ is the carrier wavelength. The network geometry is modeled on a two-dimensional plane. Hence, the boresight angle of the ULA is denoted by $\psi_n \in [0, 2\pi)$ and the location of AP n , denoted by $\mathbf{s}_n = (x_n, y_n)$. Both ψ_n and \mathbf{s}_n for all $n \in \mathcal{N}$ assumed to be known at the ES, while the unknown target location $\mathbf{q} = (x_t, y_t)$ is estimated from the sensing measurements.

A. Frame Structure

The SNs operate over an orthogonal frequency-division multiple access (OFDMA) discrete time–frequency grid with N_{sc} subcarriers spaced in frequency by Δf , starting from the lowest frequency f_0 . Accordingly, the total transmission bandwidth is given by $W = N_{sc}\Delta f$, and the frequency of the k -th subcarrier is expressed as $f_k = f_0 + k\Delta f$, where $k \in \{0, 1, \dots, N_{sc} - 1\}$. The frame of duration T is divided into F time slots of equal length, where each slot contains multiple symbols and spans the system bandwidth. The ES is connected to the 6G network to ensure global synchronization while also orchestrating network-level resource allocation across SNs. The allocation is carried out at the OFDM-symbol level, with each symbol assigned exclusively to either sensing or communication. To prevent mutual interference during sensing, each sensing symbol is exclusively assigned to a single SN, while the remaining SNs refrain from transmissions, and may operate in receive mode to collect echoes.

Without loss of generality, the localization process is performed over one or more sensing iterations within a total time budget T_c , which is assumed to be sufficiently short such that the target motion is negligible. Each iteration consists of a *sensing phase* and a *feedback phase*. During each sensing phase, one SN acts as the probing transmitter, while the others operate in echo-reception mode or remain idle. During each feedback phase, the echo-receiving SNs report their measurements to the ES via an out-of-band control channel for centralized fusion and target localization. If further refinement is required, the ES triggers the next iteration by broadcasting the updated configuration, including the sensing symbol allocation and the designated transmitting and receiving subsets; otherwise, the localization process is terminated. Accordingly, the number of sensing iterations determines the portion of OFDM frame resources reallocated from communication to sensing.

III. SENSING FRAMEWORK

The SN APs perform multi-static sensing, where at each sensing iteration, one SN $i \in \mathcal{N}$ acts as the illuminator (Tx) and a subset $\mathcal{J}_i \subseteq \mathcal{N} \setminus \{i\}$ acts as echo receivers (Rx). During sensing, the Tx transmits known pilots $X_i[k]$ on occupied subcarriers. After OFDM demodulation, the received pilot sample at Rx $j \in \mathcal{J}_i$ on subcarrier k and antenna m is

$$Y_{i,j}[k, m] = X_i[k] H_{i,j}[k, m] + N_j[k, m], \quad (1)$$

where $\mathbf{H}_{i,j} \in \mathbb{C}^{N_{sc} \times M_a}$ is the bistatic echo channel coefficient and $N_j[k, m] \sim \mathcal{CN}(0, \sigma_n^2)$ is the thermal noise with power $\sigma_n^2 = k_B T_n F_n \Delta f$, where k_B is the Boltzmann's constant, T_n is the noise temperature, and F_n is the receiver noise figure. Using per-tone least square (LS) estimation, we obtain

$$\hat{H}_{i,j}[k, m] = H_{i,j}[k, m] + W_{i,j}[k, m], \quad (2)$$

where $W_{i,j}[k, m] = N_j[k, m]/X_i[k]$ is the channel-estimation error. Under equal per-tone pilot power $P_{\text{tone}} = |X_i[k]|^2$, the entries of $\mathbf{W}_{i,j}$ are i.i.d. $\mathcal{CN}(0, \sigma_H^2)$ with $\sigma_H^2 = \sigma_n^2/P_{\text{tone}}$.

The industrial environment contains widely distributed static scatterers. Therefore, the echo channel is decomposed into the intended target component $\mathbf{H}_{i,j}^{(T)}$ and an aggregate clutter component $\mathbf{H}_{i,j}^{(C)}$, with the line of sight (LOS) path embedded in both, as

$$\mathbf{H}_{i,j} = \mathbf{H}_{i,j}^{(T)} + \mathbf{H}_{i,j}^{(C)}. \quad (3)$$

Denote the set of static clutter scatterers by $\{\mathbf{c}_\ell\}_{\ell \in C}$. For a generic scatterer at $\mathbf{p} = (r_p, \theta_p) \in \{\mathbf{q}\} \cup \{\mathbf{c}_\ell\}_{\ell \in C}$, let $d_i(\mathbf{p}) \triangleq \|\mathbf{p} - \mathbf{s}_i\|$ and $d_j(\mathbf{p}) \triangleq \|\mathbf{p} - \mathbf{s}_j\|$ denote the Tx–scatterer and scatterer–Rx distances. The bistatic delay is

$$\tau_{i,j}(\mathbf{p}) \triangleq \frac{d_i(\mathbf{p}) + d_j(\mathbf{p})}{c}, \quad (4)$$

where c is the speed of light. The AoA relative to the Rx boresight is

$$\vartheta_j(\mathbf{p}) \triangleq \text{wrap}_{[-\pi, \pi)}\left(\text{atan2}(\mathbf{p} - \mathbf{s}_j, \mathbf{p} - \mathbf{s}_j) - \psi_j\right), \quad (5)$$

where $\text{wrap}_{[-\pi, \pi)}(\cdot)$ maps its argument to $[-\pi, \pi)$.

For the ULA at SN j , with centered element index $\tilde{m} \triangleq m - \frac{M_a-1}{2}$, the wideband steering response on subcarrier k for an impinging angle ϑ is given by

$$[a_j(f_k, \vartheta)]_m \triangleq \exp\left(-j2\pi \frac{f_k}{c} d \sin(\vartheta) \tilde{m}\right). \quad (6)$$

With single-bounce scattering, the contribution of scatterer \mathbf{p} to the (k, m) th channel entry is modeled as

$$H_{i,j}^{(\mathbf{p})}[k, m] = \gamma(\mathbf{p}) e^{-j2\pi f_k \tau_{i,j}(\mathbf{p})} [a_j(f_k, \vartheta_j(\mathbf{p}))]_m, \quad (7)$$

where $\gamma(\mathbf{p})$ according to the bistatic radar equation, is $\gamma(\mathbf{p}) = \sqrt{G_i G_j \lambda^2 \sigma(\mathbf{p})} / (4\pi)^3 (d_i(\mathbf{p}) d_j(\mathbf{p}))^{-1}$, where (G_i, G_j) denote the antenna gains and $\sigma(\mathbf{p})$ is the radar RCS, and follows the Swerling-I model [8] with mean σ_0 . Summing (7) over the target and clutter scatterers yields $\mathbf{H}_{i,j}^{(\text{T})}$ and $\mathbf{H}_{i,j}^{(\text{C})}$ in (3).

A. Clutter Suppression via Background Learning

The clutter term $\mathbf{H}_{i,j}^{(\text{C})}$ can obscure $\mathbf{H}_{i,j}^{(\text{T})}$. Therefore, learning and suppressing $\mathbf{H}_{i,j}^{(\text{C})}$ is crucial for reliable detection, avoiding false alarms, and unbiased parameter extraction.

The background response is not geometry-agnostic; changing the ordered bistatic pair (i, j) generally yields a different clutter channel $\mathbf{H}_{i,j}^{(\text{C})}$ due to the change in Tx/Rx locations, which necessitates repeated background learning and incurs substantial time and spectral overhead. To address this, we exploit the fact that, in many industrial deployments, SNs operate from a finite set of feasible locations. Let $\mathcal{L} = \{1, \dots, L\}$ denote the location set, and let $\pi: \mathcal{N} \rightarrow \mathcal{L}$ map each SN index to its operating location. Under this discrete-location model, the background clutter is determined by the ordered location pair $(t, r) = (\pi(i), \pi(j))$. Thus, we define a geometry-consistent dictionary $\mathcal{D}: \mathcal{L} \times \mathcal{L} \rightarrow \mathbb{C}^{N_{\text{sc}} \times M_a}$, where $(t, r) \mapsto \hat{\mathbf{H}}_{t,r}^{\text{bg}}$ denotes the learned target-free background channel, with generally $\hat{\mathbf{H}}_{t,r}^{\text{bg}} \neq \hat{\mathbf{H}}_{r,t}^{\text{bg}}$. In practice, \mathcal{D} can be stored at the ES and periodically distributed to SNs; each receiver then performs clutter suppression by simple dictionary lookup using its own location and the active Tx location.

To populate the dictionary \mathcal{D} , a preprocessing stage is performed prior to any localization task by the ES. Let N_{BG} denote the number of target-free symbols used to learn one dictionary entry. Calibration is performed sequentially over feasible transmit locations; for each $t \in \mathcal{L}$, a node operating at location t transmits pilots once while receivers at all other locations $r \in \mathcal{L} \setminus \{t\}$ collect target-free observations simultaneously. Hence, the set of entries $\{\hat{\mathbf{H}}_{t,r}^{\text{bg}}\}_{r \neq t}$ is obtained. Denoting the resulting matrices by $\{\hat{\mathbf{H}}_{t,r}^{\text{bg},(n)}\}_{n=1}^{N_{\text{BG}}}$, we compute a robust background estimate via the complex median

$$\hat{\mathbf{H}}_{t,r}^{\text{bg}} \triangleq \text{med}_n\left(\Re\{\hat{\mathbf{H}}_{t,r}^{\text{bg},(n)}\}\right) + j \text{med}_n\left(\Im\{\hat{\mathbf{H}}_{t,r}^{\text{bg},(n)}\}\right), \quad (8)$$

and store it as the dictionary entry $\mathcal{D}(t, r) \triangleq \hat{\mathbf{H}}_{t,r}^{\text{bg}}$. The resulting dictionary can subsequently be employed for clutter suppression across localization tasks and updated over time to reflect changes in the clutter environment.

During sensing, receiver j first obtains $\tilde{\mathbf{H}}_{i,j}$ from the LS estimate and then retrieves the geometry-consistent background

$\hat{\mathbf{H}}_{\pi(i), \pi(j)}^{\text{bg}} = \mathcal{D}(\pi(i), \pi(j))$. The clutter-suppressed residual channel is therefore

$$\begin{aligned} \tilde{\mathbf{H}}_{i,j} &\triangleq \hat{\mathbf{H}}_{i,j} - \hat{\mathbf{H}}_{\pi(i), \pi(j)}^{\text{bg}} \\ &= \mathbf{H}_{i,j}^{(\text{T})} + \underbrace{(\mathbf{H}_{i,j}^{(\text{C})} - \hat{\mathbf{H}}_{\pi(i), \pi(j)}^{\text{bg}})}_{\text{residual clutter}} + \tilde{\mathbf{W}}_{i,j}, \end{aligned} \quad (9)$$

where $\tilde{\mathbf{W}}_{i,j}$ aggregates the sensing-snapshot LS error and the median-attenuated calibration noise in the dictionary entry.

B. Range–Angle Power Map, Detection, and Refinement

Given the background-suppressed residual channel $\tilde{\mathbf{H}}_{i,j} \in \mathbb{C}^{N_{\text{sc}} \times M_a}$, we construct a range–angle power map that highlights target-induced peaks. Let $\tilde{\mathbf{h}}_{i,j}[k] \triangleq [\tilde{\mathbf{H}}_{i,j}]_{k,:}^T \in \mathbb{C}^{M_a \times 1}$ denote the spatial snapshot on subcarrier k . The receiver performs beam sweeping over a predefined grid of candidate angles $\Theta = \{\vartheta_g\}_{g=1}^{N_\vartheta}$. For each ϑ_g , wideband matched receive combining across the ULA using the steering vector $\mathbf{a}_j(f_k, \vartheta_g) \in \mathbb{C}^{M_a \times 1}$, yields

$$z_{i,j}[k; \vartheta_g] \triangleq \frac{1}{\sqrt{M_a}} \mathbf{a}_j^\dagger(f_k, \vartheta_g) \tilde{\mathbf{h}}_{i,j}[k], \quad (10)$$

where $(\cdot)^\dagger$ is the Hermitian transpose. The angle-conditioned delay profile is then obtained by delay compression across subcarriers, i.e., $Z_{i,j}[\ell; \vartheta_g] = \text{IFFT}_k\{z_{i,j}[k; \vartheta_g]\}$ for $\ell = 0, \dots, N_{\text{sc}} - 1$. This yields a sampled delay response with bin spacing $\Delta\tau = 1/(N_{\text{sc}}\Delta f)$, corresponding to bistatic range $\rho_\ell = c\ell\Delta\tau$. The resulting range–angle power map is

$$P_{i,j}[g, \ell] \triangleq |Z_{i,j}[\ell; \vartheta_g]|^2. \quad (11)$$

Collecting $P_{i,j}[g, \ell]$ over all angle and delay bins yields $\mathbf{P}_{i,j} \in \mathbb{R}_+^{N_\vartheta \times N_{\text{sc}}}$. For each sensing link, the range–angle power map $\mathbf{P}_{i,j}$ is processed using an edge-aware 2-D CA-CFAR detector [9] to identify candidate angle–range bins and extract coarse hypotheses for subsequent localization. The resulting detections are further pruned using non-maximum suppression (NMS) technique to avoid multiple detections from the same peak region, yielding the candidate set $\mathcal{K}_{i,j}$. For each candidate $(g_0, \ell_0) \in \mathcal{K}_{i,j}$ with coarse angle ϑ_{g_0} and coarse delay $\tau_0 = \ell_0\Delta\tau$, the AoA is refined via MUSIC-based angular super-resolution [10], while the ToA is refined from the linear phase trend across subcarriers, yielding a refined AoA–ToA pair $(\hat{\vartheta}_{i,j}, \hat{\tau}_{i,j})$.

IV. DATA FUSION

For each active sensing link (i, j) , receiver j reports the ToA estimate $\hat{\tau}_{i,j}$, the AoA estimate $\hat{\vartheta}_{i,j}$, and the corresponding eCRLBs as reliability indicators to the ES. These eCRLBs are computed from the detected-cell power and a robust estimate of the noise floor on the range–angle map. Specifically, let $P_{i,j}^{\text{det}} \triangleq P_{i,j}[g_0, \ell_0]$ denote the power of the selected detection, and let $\hat{P}_{i,j}^{\text{n}} \triangleq \text{median}\{P_{i,j}[g, \ell]\}_{g,\ell}$ denote a robust estimate of the noise floor. Based on these quantities, we define the SNR proxy $\hat{\gamma}_{i,j} \triangleq P_{i,j}^{\text{det}} / (\hat{P}_{i,j}^{\text{n}} + \epsilon)$ and the corresponding ToA variance [11] is approximated as $\sigma_{\tau,i,j}^2 \triangleq (2\pi W_{\text{rms}} \sqrt{2\hat{\gamma}_{i,j}})^{-2}$ with $W_{\text{rms}} \triangleq \sqrt{\frac{1}{N_{\text{sc}}} \sum_k f_k^2}$.

Likewise, the AoA variance [10] is approximated as $\sigma_{\vartheta,i,j}^2 \triangleq 6 \left(N_s \widehat{\gamma}_{i,j} (2\pi d/\lambda)^2 M_a (M_a^2 - 1) \cos^2(\widehat{\vartheta}_{i,j}) \right)^{-1}$. The ES then estimates the target location \mathbf{q} via nonlinear WLS

$$\mathbf{P1:} \quad \min_{\mathbf{q}} \sum_{j \in \mathcal{J}_i^{\tau}} \frac{(\widehat{\tau}_{i,j} - \tau_{i,j}(\mathbf{q}))^2}{\sigma_{\tau,i,j}^2} + \sum_{j \in \mathcal{J}_i^{\vartheta}} \frac{(\text{wrap}_{[-\pi,\pi]}(\widehat{\vartheta}_{i,j} - \vartheta_j(\mathbf{q})))^2}{\sigma_{\vartheta,i,j}^2}, \quad (12)$$

where \mathcal{J}_i^{τ} and $\mathcal{J}_i^{\vartheta}$ denote the sets of receivers that provide admitted ToA and AoA measurements, respectively. Problem **P1** is a nonlinear WLS problem that can be efficiently solved by Gauss–Newton iterations [2].

V. ITERATIVE ADAPTIVE SENSING, LOCALIZATION, AND NODE-SELECTION PLANNING

The ES executes the sensing–localization pipeline iteratively. At the initial iteration, no estimate of the target location is available. Therefore, selecting the Tx–Rx subset based on a random assumed target point can bias the algorithm toward a weak initial geometry and degrade the subsequent updates. To mitigate this, we adopt a sampling-based FoV-aware initialization (SFI). Specifically, N_s sample points are uniformly drawn over the target search area, and the initial receiver subset is chosen to maximize their FoV coverage

$$\mathcal{J}^{(1)*} := \arg \max_{\substack{\mathcal{J} \subseteq \mathcal{N} \\ |\mathcal{J}|=N_r}} \sum_{s=1}^{N_s} \mathbf{1}(\exists j \in \mathcal{J} : I_{j,s} = 1), \quad (13)$$

where $I_{j,s} = 1$ if sample point s lies inside the FoV of receiver j and 0 otherwise. Thus, the initial receiver subset is chosen to maximize geometric visibility over the target search area. Given $\mathcal{J}^{(1)*}$, the initial transmitter is selected to minimize the average empirical PEB over the same sample points as

$$i^{(1)*} := \arg \min_{i \in \mathcal{N} \setminus \mathcal{J}^{(1)*}} \frac{1}{|\mathcal{X}_{\text{use}}|} \sum_{\mathbf{q} \in \mathcal{X}_{\text{use}}} \text{PEB}(\mathbf{q}; i, \mathcal{J}^{(1)*}), \quad (14)$$

where \mathcal{X}_{use} denotes the sampled area points, and $\text{PEB}(\cdot)$ denotes the empirical localization-quality metric, whose explicit expression is given later in (18). The resulting configuration $(i^{(1)*}, \mathcal{J}^{(1)*})$ is then used to obtain the first target-location estimate $\widehat{\mathbf{q}}^{(1)}$ by solving Problem **P1**.

At iteration $j > 1$, the ES uses the current estimate $\widehat{\mathbf{q}}^{(j)}$ to select the next multi-static sensing configuration. Specifically, it selects the transmitter $i^{(j+1)} \in \mathcal{N}$ and the receiver subset $\mathcal{J}^{(j+1)} \subseteq \mathcal{N} \setminus \{i^{(j+1)}\}$, with $|\mathcal{J}^{(j+1)}| = N_r$, that yield the smallest predicted PEB, defined later in Problem **P2**. The selected nodes then perform a new sensing measurements, and report them to the ES for data fusion and refining the target-location estimate to $\widehat{\mathbf{q}}^{(j+1)}$ by solving Problem **P1**.

This iterative procedure continues until the sensing reconfiguration remains unchanged over two consecutive iterations, that is, when $i^{(j+1)} = i^{(j)}$ and $\mathcal{J}^{(j+1)} = \mathcal{J}^{(j)}$. The overall procedure of PEB-based sensing reconfiguration (PEB-SR) is summarized in Algorithm 1.

Algorithm 1: PEB-Based Sensing Reconfiguration (PEB-SR) for Cooperative Localization

Input: SN locations and boresights $\{(s_n, \psi_n)\}_{n=1}^N$, Rx set cardinality $|\mathcal{J}| = N_r$, max. no. of reconfigurations J_{max} , max. no. of WLS iterations L_{max} , threshold ε .

Output: Estimated location $\widehat{\mathbf{q}}^*$, selected configuration (i^*, \mathcal{J}^*) .

- 1 **Initialize:** Select an initial sensing configuration $(i^{(1)}, \mathcal{J}^{(1)})$ via (13), and (14); initialize $\widehat{\mathbf{q}}$; set $j \leftarrow 1$;
- 2 **while** $j < J_{\text{max}}$ **do**
- 3 **Sensing:** Activate Tx $i^{(j)}$ and receivers $\mathcal{J}^{(j)}$;
- 4 **foreach** $r \in \mathcal{J}^{(j)}$ **do**
- 5 Receiver r estimates ToA and uncertainty $(\widehat{\tau}_{i^{(j)},r}, \sigma_{\tau,i^{(j)},r}^2)$;
- 6 Receiver r estimates AoA and uncertainty $(\widehat{\vartheta}_{i^{(j)},r}, \sigma_{\vartheta,i^{(j)},r}^2)$;
- 7 Send measured values to the ES;
- 8 **Data fusion (P1 at ES):** Initialize $\mathbf{q}^{(0)} \leftarrow \widehat{\mathbf{q}}$;
- 9 **for** $\ell \leftarrow 1$ **to** L_{max} **do**
- 10 Update $\mathbf{q}^{(\ell)}$ by one Gauss–Newton WLS step in **P1**;
- 11 **if** $\|\mathbf{q}^{(\ell)} - \mathbf{q}^{(\ell-1)}\| \leq \varepsilon$ **then**
- 12 **break**;
- 13 Set $\widehat{\mathbf{q}} \leftarrow \mathbf{q}^{(\ell)}$;
- 14 $j \leftarrow j + 1$;
- 15 **PEB-based configuration selection (P2 at ES):** Evaluate $\text{PEB}(i, \mathcal{J})$ for all $i \in \mathcal{N}$ and $\mathcal{J} \subseteq \mathcal{N} \setminus \{i\}$ using $\widehat{\mathbf{q}}$ via (19);
- 16 $(i^{(j)}, \mathcal{J}^{(j)}) \leftarrow \arg \min \text{PEB}(i, \mathcal{J})$;
- 17 **if** $(i^{(j)}, \mathcal{J}^{(j)}) = (i^{(j-1)}, \mathcal{J}^{(j-1)})$ **then**
- 18 **break**;
- 19 **return** $(i^*, \mathcal{J}^*) \leftarrow (i^{(j)}, \mathcal{J}^{(j)})$, $\widehat{\mathbf{q}}^* \leftarrow \widehat{\mathbf{q}}$;

To schedule the next sensing iteration, the ES evaluates all possible sensing configurations using the current estimate $\widehat{\mathbf{q}}^{(j)}$. In fact, $\widehat{\mathbf{q}}^{(j)}$ serves as a proxy target location for predicting the geometric sensitivity and measurement reliability of candidate links that were inactive in the previous iteration. For simplicity, we denote $\widehat{\mathbf{q}} \triangleq \widehat{\mathbf{q}}^{(j)}$. For a candidate bistatic link (i, j) , the gradient of the bistatic delay in (4), evaluated at $\widehat{\mathbf{q}}$, is

$$\mathbf{g}_{\tau,i,j}(\widehat{\mathbf{q}}) = \nabla_{\mathbf{q}} \tau_{i,j}(\mathbf{q}) \Big|_{\mathbf{q}=\widehat{\mathbf{q}}} = \frac{1}{c} \left(\frac{\widehat{\mathbf{q}} - \mathbf{s}_i}{d_i(\widehat{\mathbf{q}})} + \frac{\widehat{\mathbf{q}} - \mathbf{s}_j}{d_j(\widehat{\mathbf{q}})} \right). \quad (15)$$

Likewise, the gradient of the AoA in (5), evaluated at $\widehat{\mathbf{q}}$, is

$$\mathbf{g}_{\vartheta,j}(\widehat{\mathbf{q}}) = \nabla_{\mathbf{q}} \vartheta_j(\mathbf{q}) \Big|_{\mathbf{q}=\widehat{\mathbf{q}}} = \frac{1}{\|\widehat{\mathbf{q}} - \mathbf{s}_j\|^2} \begin{bmatrix} -(\widehat{q}_y - s_{j,y}) \\ (\widehat{q}_x - s_{j,x}) \end{bmatrix}. \quad (16)$$

Using the bistatic radar-equation scaling, the per-tone channel-amplitude proxy at $\widehat{\mathbf{q}}$ is modeled as $\alpha_{i,j}(\widehat{\mathbf{q}}) = \sqrt{G_i G_j \lambda^2 \sigma(\widehat{\mathbf{q}}) / (4\pi)^3} (d_i(\widehat{\mathbf{q}}) d_j(\widehat{\mathbf{q}}))^{-1}$, and the proxy per-tone SNR is then defined as $\widetilde{\gamma}_{i,j} \triangleq \alpha_{i,j}^2(\widehat{\mathbf{q}}) / \sigma_H^2$. Given $\widetilde{\gamma}_{i,j}$, the predicted ToA and AoA measurement variances, denoted by $\sigma_{\tau,i,j}^2(\widehat{\mathbf{q}})$ and $\sigma_{\vartheta,i,j}^2(\widehat{\mathbf{q}})$, respectively, are obtained using the same models as in Problem **P1**. Accordingly, the predicted Fisher-information contribution of link (i, j) is

$$\mathbf{J}_{i,j}(\widehat{\mathbf{q}}) \triangleq \frac{1}{\sigma_{\tau,i,j}^2(\widehat{\mathbf{q}})} \mathbf{g}_{\tau,i,j}(\widehat{\mathbf{q}}) \mathbf{g}_{\tau,i,j}^{\top}(\widehat{\mathbf{q}}) + \frac{1}{\sigma_{\vartheta,i,j}^2(\widehat{\mathbf{q}})} \mathbf{g}_{\vartheta,j}(\widehat{\mathbf{q}}) \mathbf{g}_{\vartheta,j}^{\top}(\widehat{\mathbf{q}}). \quad (17)$$

By the additive property of Fisher information, the total predicted information for a candidate configuration (i, \mathcal{J}) is $\mathbf{J}_{i, \mathcal{J}}(\hat{\mathbf{q}}) \triangleq \sum_{j \in \mathcal{J}} \mathbf{J}_{i, j}(\hat{\mathbf{q}})$. Accordingly, the regularized information matrix is formed as $\mathbf{A}_{i, \mathcal{J}} \triangleq \mathbf{J}_{i, \mathcal{J}}(\hat{\mathbf{q}}) + \mu_{\text{reg}} \mathbf{I}_2$, where $\mu_{\text{reg}} > 0$ is a small regularization constant, and the candidate configuration is scored by the empirical PEB,

$$\text{PEB}(i, \mathcal{J}) \triangleq \sqrt{\text{tr}(\mathbf{A}_{i, \mathcal{J}}^{-1})}. \quad (18)$$

The next sensing configuration is then selected by solving **P2**,

$$\mathbf{P2}: (i^*, \mathcal{J}^*) := \arg \min_{\substack{i \in \mathcal{N}, \mathcal{J} \subseteq \mathcal{N} \setminus \{i\} \\ |\mathcal{J}| = N_r}} \text{PEB}(i, \mathcal{J}). \quad (19)$$

The next sensing iteration is scheduled using i^* and \mathcal{J}^* . Problem **P2** is combinatorial; however, exhaustive search remains computationally feasible for moderate values of $|\mathcal{N}|$ and N_r .

VI. NUMERICAL RESULTS AND DISCUSSION

In this section, we evaluate the proposed scheme in an IIoT scenario where one target, $N = 40$ SNs, and $N_{\text{cl}} = 30$ dedicated clutter scatterers are uniformly distributed over a $200 \times 200 \text{ m}^2$ area, with the SNs also treated as additional clutter sources. The carrier frequency is 10 GHz, the transmit power is $p_n = 23 \text{ dBm}$, the mean target/clutter RCS is $\sigma_0 = 0 \text{ dBsm}$, and the transmit and receive antenna gains are $G_t = G_r = 0 \text{ dBi}$, with boresight angle $\psi_n \sim \mathcal{U}[0, 2\pi)$. The frame structure follows 5G NR numerology 0, with frame duration $T = 10 \text{ ms}$, $F = 10$ slots per frame, and 14 OFDM symbols per slot. The bandwidth is $W = 100 \text{ MHz}$. The number of background-learning symbols is set to $N_{\text{BG}} = 70$, and the noise power spectral density is -174 dBm/Hz .

We compare the proposed scheme with three reference variants, three benchmark schemes, and two theoretical bounds. The reference variants are the proposed scheme with no clutter suppression (PS–NCS), assuming clutter-free conditions (PS–CF), and omitting SFI (PS–NSFI). The benchmarks and the theoretical bounds are:

- **Random Subset Averaging (RSA)**: an iterative scheme in which the first subset is selected using SFI and the next subsets are chosen randomly. The final estimate is obtained by averaging the intermediate estimates.
- **Fixed Initialized Subset (FIS)**: a single-shot scheme using the subset selected by SFI.
- **Oracle Best Subset (OBS)**: a single-shot scheme that assumes perfect knowledge of the true target location and selects the optimal sensing subset from (19).
- **OBS-PEB**: a single-shot theoretical lower bound, corresponding to the OBS, obtained via (18).
- **SFI-PEB**: a single-shot theoretical lower bound, corresponding to the subset selected by SFI, obtained via (18).

For a fair comparison, the proposed method and the RSA use one sensing symbol per iteration over J_{max} iterations, while each single-shot benchmark is assigned the same total budget of J_{max} symbols, in a single sensing iteration.

Fig. 2 shows the empirical RMSE and corresponding PEB versus J_{max} for the bi-static setup with $M_a = 32$ antennas.

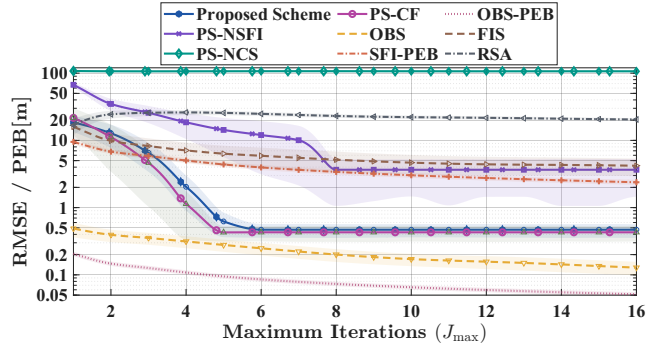


Fig. 2: Accuracy of the proposed method against benchmark schemes.

The shaded regions denote the 90% confidence intervals. The proposed scheme rapidly reduces the localization RMSE from about 20 m at $J_{\text{max}} = 1$ to about 0.45 m at $J_{\text{max}} = 6$, after which the performance saturates. The PS–CF variant follows a similar trend, with only slightly lower RMSE during the transient regime, indicating that the proposed clutter-suppression method effectively recovers clutter-free accuracy. In contrast, the PS–NCS variant remains close to 100 m over the entire range of J_{max} , confirming that clutter suppression is essential. The PS–NSFI variant converges more slowly and to a much higher error floor, decreasing from about 67 m to only 3.6 m, with a wider 90% confidence interval that indicates greater sensitivity to the initial SN choice. This trend highlights the importance of SFI when no prior information about the target location is yet available. Among the benchmark schemes, OBS achieves the best empirical localization performance. However, since it assumes perfect knowledge of the target location for subset selection, it should be regarded as an optimistic lower reference rather than a realizable scheme. At $J_{\text{max}} = 6$, OBS achieves an RMSE of about 0.25 m, only about 0.2 m below the proposed method; this remaining gap is mainly due to oracle-aided subset selection and one-shot use of the full sensing budget. The FIS improves monotonically with J_{max} , with its RMSE decreasing from about 20 m to 4.2 m, while the corresponding SFI-PEB stays lower and decreases from about 10 m to 2.4 m. By contrast, RSA exhibits non-monotonic behavior. Although it initially benefits from the proposed SFI scheme, subsequent random subset updates increase the RMSE over the next few iterations before averaging reduces it again. Overall, the combination of SFI and PEB-based node refinement yields a nearly two orders-of-magnitude RMSE reduction in six iterations, the lowest error among realizable benchmarks, and the smallest gap to OBS.

Table I reports the percentile localization error at convergence for different (M_a, N_r) configurations. Increasing M_a consistently improves performance across all percentiles, reflecting the benefit of larger arrays for more accurate AoA estimation. By contrast, the impact of increasing N_r is non-monotonic and percentile-dependent: it generally improves the upper tail of the error distribution, e.g., the 95th percentile, by reducing large-error events through multistatic diversity, but does not uniformly improve the lower and central percentiles,

TABLE I: Localization RMSE for different (M_a, N_r) configurations.

Percentile (%)	$M_a = 4$			$M_a = 16$		
	$N_r = 1$	$N_r = 2$	$N_r = 3$	$N_r = 1$	$N_r = 2$	$N_r = 3$
25	0.0198	0.0101	0.0268	0.0056	0.0083	0.0116
50	0.1408	0.2615	0.3200	0.0107	0.0173	0.0198
75	0.4481	0.9036	0.8037	0.0215	0.0556	0.0646
90	1.4493	1.7943	1.3402	0.3281	0.2267	0.2416
95	4.7151	2.2916	1.7872	0.6050	0.5730	0.4130

since additional receivers may provide weak or geometrically unfavorable observations. This suggests that adaptive N_r selection based on sensing geometry and measurement quality is a promising direction for future work.

Fig. 3 reports the simulation runtime until convergence of the single-link-sensing and SN selection stages for different (M_a, N_r) configurations. All results were obtained using MATLAB 2025 on a Windows 11 desktop with an Intel Core Ultra 7 155U CPU at 1.70 GHz, and thus are intended only for relative comparison across configurations, rather than as absolute execution times on optimized software or dedicated hardware. In a real implementation, the sensing-link computations are performed locally at the selected SNs, whereas SN selection and data fusion are performed at the ES. The data-fusion time is omitted because it is negligible compared to the other two stages. As shown in Fig. 3, increasing M_a from 4 to 16 reduces the iterations needed for convergence, but increases the single-link sensing time. Hence, for $N_r = 1, 2$, the total runtime remains higher for $M_a = 16$, whereas for $N_r = 3$, where SN selection time dominates, the faster convergence of the larger array reduces the total runtime below that of $M_a = 4$. Moreover, increasing N_r has little effect on single-link-sensing time due to parallel sensing across selected receivers, but substantially increases the ES-side SN-selection time. Together with Table I, this reveals an accuracy-latency tradeoff: larger arrays improve localization accuracy, while more receivers mainly improve upper-tail accuracy at the cost of higher latency and resource usage.

With the assumption that a sensing interval spans one OFDM symbol, if all sensing iterations are completed within a single frame, the throughput loss is $\eta_{\text{loss}}(\%) = \frac{J_{\text{max}}}{140} \times 100 = 0.7143J_{\text{max}}$. Based on the average number of convergence iterations \bar{J}_{max} , the throughput loss increases from 2.35% to 2.64% for $M_a = 16$ and from 3.28% to 3.5% for $M_a = 4$ as N_r increases from 1 to 3. Together with Table II, this shows that larger arrays improve localization accuracy while reducing the communication penalty by accelerating convergence. In contrast, moving from the bi-static to the multi-static setup improves upper-tail localization accuracy at the expense of a slight increase in η_{loss} due to the larger average number of convergence iterations. Nevertheless, the throughput loss remains below 3.5% for all considered configurations.

VII. CONCLUSIONS AND FUTURE WORK

We proposed a novel ISAC framework for collaborative multi-static target localization in cluttered IIoT environments. The proposed solution periodically learns the background clutter response and suppresses it before target sensing. For

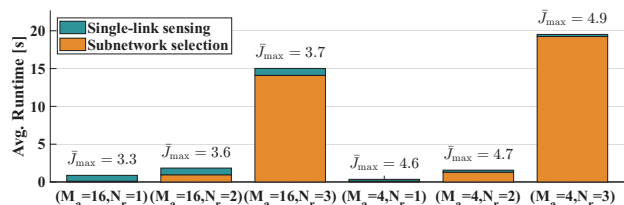


Fig. 3: Average runtime of the SN-selection and single-link-sensing stages.

target localization, it first uses a sampling-based FoV-aware initialization scheme to improve geometric visibility toward the target. Then, an empirical PEB-based node refinement scheme is applied to adaptively select the most informative sensing nodes, thus improving localization accuracy with limited resource-latency budget. Numerical results show that clutter suppression is essential, with the proposed method achieving near-clutter-free performance. The proposed method reduces the localization RMSE by nearly two orders of magnitude to about 45 cm, outperforming all considered benchmarks and approaching the oracle best-subset benchmark. Increasing the number of antennas improves localization accuracy and accelerates convergence, while the impact of the number of multi-static receivers is non-monotonic; the communication throughput loss remains below 3.5% across all considered configurations. Future work will consider adaptive selection of the number of multi-static receivers and joint sensing-communication design under stringent QoS requirements.

ACKNOWLEDGMENTS

This work is supported by Independent Research Fund Denmark, grant no. 3105-00077B.

REFERENCES

- [1] G. Berardinelli *et al.*, “Extreme communication in 6G: Vision and challenges for ‘in-X’ subnetworks,” *IEEE Open J. Commun. Soc.*, vol. 2, pp. 2516–2535, 2021.
- [2] M. Nozari *et al.*, “Toward ISAC-empowered subnetworks: Cooperative localization and iterative node selection,” in *Proc. IEEE Global Communications Conference (GLOBECOM) Workshops*, 2025.
- [3] H. Li *et al.*, “Multi-node multi-band cooperative integrated sensing and communications: State-of-the-art, challenges and opportunities,” *IEEE Wireless Commun.*, vol. 32, no. 4, pp. 180–188, 2025.
- [4] X. Du *et al.*, “Multi-agent reinforcement learning for dynamic resource management in 6G in-X subnetworks,” *IEEE Transactions on Wireless Communications*, vol. 22, no. 3, pp. 1900–1914, 2022.
- [5] D. Abode *et al.*, “Goal-oriented interference coordination in 6G in-factory subnetworks,” *IEEE Journal on Selected Areas in Communications*, vol. 43, no. 9, pp. 3088–3103, 2025.
- [6] Z. Behdad *et al.*, “Power allocation for joint communication and sensing in cell-free massive MIMO,” in *Proc. IEEE Global Communications Conference (GLOBECOM)*, 2022, pp. 4081–4086.
- [7] Y. Wang *et al.*, “Dynamic target sensing for ISAC systems in clutter environment,” in *Proc. IEEE Wireless Communications and Networking Conference (WCNC)*, 2024.
- [8] P. Swerling, “Probability of detection for fluctuating targets,” *IRE Transactions on Information theory*, vol. 6, no. 2, pp. 269–308, 2003.
- [9] H. Rohling, “Radar CFAR thresholding in clutter and multiple target situations,” *IEEE Transactions on Aerospace and Electronic Systems*, no. 4, pp. 608–621, 2007.
- [10] A. Xhafa *et al.*, “Experimental investigation of AoA estimation and antenna calibration with 5G NR signals using USRP devices,” *IEEE Transactions on Instrumentation and Measurement*, vol. 74, 2025.
- [11] S. Gezici and H. V. Poor, “Position estimation via ultra-wide-band signals,” *Proceedings of the IEEE*, vol. 97, no. 2, pp. 386–403, 2009.